Temporal *H*/alpha Target Decomposition for Landslide Monitoring Using Ku-Band GB-SAR Time Series

Yuta Izumi, *Student Member, IEEE*, and Motoyuki Sato, *Fellow, IEEE*

***Abstract*—We investigate the applicability of the entropy (H)/ alpha ($\bar{\alpha}$) target decomposition realized by the temporally averaged coherency matrix, called temporal $H/(\bar{\alpha})$. We apply the temporal $H/\bar{\alpha}$ to ground-based synthetic aperture radar (GB-SAR) continuous monitoring data to characterize the scattering mechanism temporal change. As a case study, this work demonstrates the application of the temporal $H/\bar{\alpha}$ technique to landslide monitoring to detect and investigate the temporal scattering mechanism. The study acquired long-term GB-SAR polarimetric data over the postlandslide slope, Minami-Aso, Kumamoto, Japan. The study first investigated the property of the temporal $H/\bar{\alpha}$ parameters over selected land cover types by comparing it with that derived by spatial averaging (spatial $H/\bar{\alpha}$) to explain the landslide monitoring results. Also, the rainfall effects on the temporal $H/\bar{\alpha}$ parameters are demonstrated. The temporal H and $\bar{\alpha}$ values increase up to 0.07° and 13.54°, respectively, when the rainfall rate is 52.5 mm/h. The time-series analysis of the temporal $H/\bar{\alpha}$ indicates an obvious temporal transition of the scattering mechanism and a change of the backscattering stationarity when a landslide occurs. The applicability of the temporal $H/\bar{\alpha}$ for the change-detection is discussed by comparing it with the classical spatial $H/\bar{\alpha}$ parameters.**

***Index Terms*—Debris avalanche, GB-SAR, ground-based synthetic aperture radar, *H*/alpha decomposition, ku-band, landslide, radar polarimetry, synthetic aperture radar.**

I. Introduction

SYNTHETIC aperture radar (SAR) is a coherent radar imaging sensor that is generally mounted on a moving platform, enabling Earth surface observation. In the last two decades, the ground-based SAR (GB-SAR) has been studied to enhance the temporal resolution and flexibility of the measurement configuration [1], [2]. A general application of GB-SAR employs the differential SAR interferometry (DInSAR) technique for land deformation monitoring. Several recent studies have shown the application of multipolarimetric measurement to realize the temporal monitoring of scattering mechanisms [3]–[6] and improve the DInSAR results [7], [8].

Manuscript received November 26, 2020; revised February 8, 2021; accepted February 15, 2021. Date of publication March 2, 2021; date of current version March 31, 2021. This work was supported in part by JSPS Grand-in-Aid for Scientific Research under Grant (A) 23246076 and in part by the Grand-in-Aid for JSPS Research Fellows under Grand 18J20104. *(Corresponding author: Yuta Izumi.)*

Yuta Izumi is with the Graduate School of Environmental Studies, Tohoku University, Sendai 980-8577, Japan (e-mail: yuta.izumi.r8@dc.tohoku.ac.jp).

Motoyuki Sato is with the Center for Northeast Asian Studies, Tohoku University, Sendai 980-8577, Japan, and also with the Graduate School of Environmental Studies, Tohoku University, Sendai 980-8577, Japan (e-mail: motoyuki.sato.b3@tohoku.ac.jp).

Digital Object Identifier 10.1109/JSTARS.2021.3062879

Multipolarimetric information can be used for the polarimetric target decomposition theorems [9]. Over naturally distributed areas, incoherent decompositions, such as eigenvector- and model-based decomposition based on polarimetric matrices (i.e., covariance or coherency matrix) provide the statistical description of the scattering mechanism variation. In the eigenvector-based decomposition, the theory is based on the derivation of the polarimetric parameters from the eigenvalues and eigenvectors of the coherency matrix proposed by Cloude [10] and Cloude and Pottier [11]. Speckle filtering must be applied before the physical interpretation of the polarimetric data realized by ensemble averaging. Therefore, the filtered coherency matrix shows second-order statistics. The derived parameters (i.e., polarimetric entropy H and mean alpha angle $\bar{\alpha}$) account for the scattering randomness and the intrinsic scattering mechanism within an ensemble. The ensemble averaging of the coherency matrix is typically performed by spatial multilooking due to insufficient polarimetric data along the temporal axis in spaceborne SAR [12].

A few studies have discussed temporal averaging's applicability in the derivation of the covariance or coherency matrix. In the spaceborne SAR context, Weissgerber *et al*. estimated the H value by temporal averaging using a temporal stack of polarimetric data [13] called temporal H (H_{temp}). However, this technique requires sufficient temporal stack polarimetric data, which is impractical in current orbital SAR missions. Furthermore, the polarimetric response has an incidence-angle dependence. Hence, temporal observations are necessary in the same position to fix the incidence angle along with the time series, which is a difficult requirement for orbital SAR. In contrast, GB-SAR measurement easily fulfills all the abovementioned requirements. Two studies in [3] and [4] used temporal averaging for the polarimetric GB-SAR measurements: one for urban monitoring and the other for glacier monitoring. However, very few cases have been reported up to now, and all the above studies discussed only the applicability of polarimetric entropy out of the other decomposition parameters via temporally averaged coherency matrix.

Considering the limited analysis in existing studies regarding polarimetric GB-SAR monitoring, we demonstrate the polarimetric decomposition technique in the continuous GB-SAR monitoring framework. We particularly focus on applying $H/\bar{\alpha}$ decomposition, derived by a temporally averaged coherency matrix referred to as the temporal $H/\bar{\alpha}$ denoted as $H_{\mathrm{temp}}/\bar{\alpha}_{\mathrm{temp}}$ to

exploit the advantage of continuous GB-SAR monitoring (i.e., a high acquisition rate and a stationary observation). Furthermore, we jointly discuss H_{temp} and $\bar{\alpha}_{\mathrm{temp}}$ parameters through the case study of landslide monitoring. In the presented analysis, the derived $H_{\mathrm{temp}}/\bar{\alpha}_{\mathrm{temp}}$ time series is further compared with conventional $H/\bar{\alpha}$ values derived by a spatially averaged coherency matrix referred to as $H_{\mathrm{spatial}}/\bar{\alpha}_{\mathrm{spatial}}$. This study contributes to the novel GB-SAR continuous monitoring approach that gives a quantitative characterization of the terrain surface temporal change and provides additional key information to the commonly used InSAR technique for more informative monitoring.

The remainder of this article is organized as follows. Section II introduces the GB-SAR monitoring campaign performed by Tohoku University over a postlandslide mountainous area. Section III elaborates on $H_{\mathrm{temp}}/\bar{\alpha}_{\mathrm{temp}}$ decomposition technique. Section IV presents the time series $H_{\mathrm{temp}}/\bar{\alpha}_{\mathrm{temp}}$ of the landslide evolution with the discussions of the properties of the both $H_{\mathrm{temp}}/\bar{\alpha}_{\mathrm{temp}}$ and $H_{\mathrm{spatial}}/\bar{\alpha}_{\mathrm{spatial}}$ parameters over the observed slope and the rainfall effect on the decomposition parameters. Section V presents the interpretation of the results in Section IV and the discussion of the comparison between the $H_{\mathrm{temp}}/\bar{\alpha}_{\mathrm{temp}}$ and $H_{\mathrm{spatial}}/\bar{\alpha}_{\mathrm{spatial}}$ results; and finally, Section VI draws the conclusions.

II. Test Site and GB-SAR System

Several landslides occurred in Kumamoto, Japan, due to a series of earthquakes in April 2016. The most noticeable landslide in Tateno, Minami-Aso, located in the caldera's outer rim, destroyed a 200 m Aso large bridge and the railroad line [14]. After the landslide occurrence, recovery projects were initiated to remove the debris flow. Considering the potential for a secondary landslide that threatened the onsite operators involved with daily road construction and the restoration work over the postlandslide slope, Tohoku University deployed polarimetric GB-SAR to monitor the slope instability [15]. The near-real-time early warning system was achieved by the continuous operational mode that repeatedly acquired the data with a 5 min temporal interval. The long-term continuous GB-SAR observation began in March 2017 and continued until August 2020.

The deployed GB-SAR system (Metasensing Fast GB-SAR) is the FMCW radar operating at the Ku-band (17.2 GHz) center frequency with a 300-MHz frequency bandwidth (see Fig. 1). This bandwidth gives a 0.5 m range resolution. The cross-range resolution is varied according to the range and computed as 4.8 mrad (4.8 m at 1000 m range). Fig. 2 depicts the observed slope steepness and plots the relative topographic height regarding the GB-SAR location over the bare surface pixels projected on the ground range axis. The GB-SAR look angle θ_{look}, slope orientation angle θ_{ori}, and local incidence angle θ_{inc} varied according to the slope location. For example, angles θ_{look}, θ_{ori}, and θ_{inc} are around 18.1°, 32.6°, and 75.4° at the 600 m ground-range, respectively.

III. Theory of Temporal H/alpha Decomposition

Cloude and Pottier introduced a scheme for parameterizing polarimetric scattering problems based on the eigenvalues and eigenvectors of the coherency matrix [10], [11], [16].

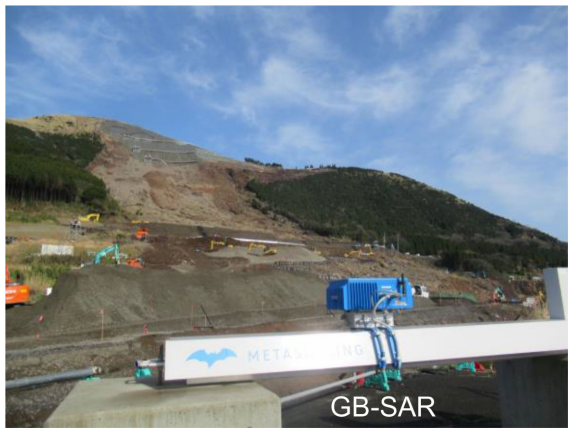

Fig. 1. Observed slope at Minami-Aso, Kumamoto, Japan, and the GB-SAR sensor.

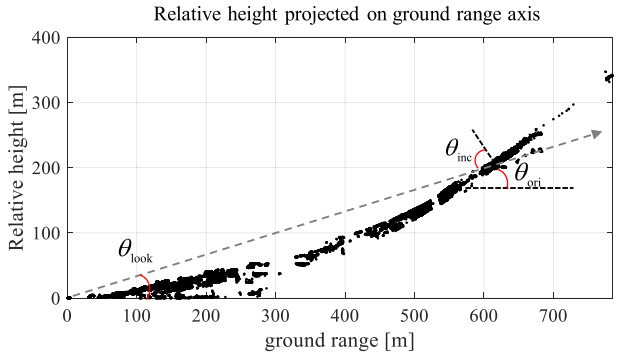

Fig. 2. Relative topographic height with reference to the GB-SAR location over the bare surface pixels projected on the ground range axis. The GB-SAR look angle θ_{look}, orientation angle θ_{ori}, and local incidence angle θ_{inc} are defined.

The 3×3 coherency matrix $\mathbf{T}$ in the monostatic case is generated by ensemble averaging of the outer product of the 3×1 Pauli scattering vector $\mathbf{k}_p$, realizing the second-order moments of the fluctuations as

$$\mathbf{T} = \left\langle \mathbf{k}_p \mathbf{k}_p^{*T} \right\rangle, \tag{1}$$

where $\langle \cdot \rangle$ denotes ensemble averaging assuming the random medium's homogeneity, and $\mathbf{k}_p^{*T}$ is the complex conjugate and transpose. The Pauli scattering vector in linear polarization basis is defined as

$$\mathbf{k}_p = \frac{1}{\sqrt{2}} \left[S_{\mathrm{HH}} + S_{\mathrm{VV}} \;\; S_{\mathrm{HH}} - S_{\mathrm{VV}} \;\; 2S_{\mathrm{HV}} \right]^T. \tag{2}$$

Decomposing the coherency matrix into the eigenvectors $\mathbf{u}_i$ and the eigenvalues λ_i, which are types of scattering processes and their relative magnitudes (used as statistical weight), respectively, we obtain

$$\mathbf{T} = \sum_{i=1}^{3} \lambda_i \mathbf{u}_i \mathbf{u}_i \;\; \lambda_1 \geq \lambda_2 \geq \lambda_3 \geq 0. \tag{3}$$

The $\mathbf{T}$ matrix is defined as the positive semidefinite Hermitian matrix; thus, the derived eigenvalues are real and positive and may have zero values. The eigenvectors in (3) are parameterized

as

$$\mathbf{u}_i = \left[\cos\alpha_i \ \sin\alpha_i \cos\beta_i e^{j\delta_i} \ \sin\alpha_i \cos\beta_i e^{j\gamma_i}\right]^T, \quad (4)$$

where phase δ_i expresses the relative phase between $S_{\mathrm{HH}} - S_{\mathrm{VV}}$ and $S_{\mathrm{HH}} + S_{\mathrm{VV}}$. Similarly, phase γ_i denotes the relative phase between S_{HV} and $S_{\mathrm{HH}} + S_{\mathrm{VV}}$. α_i represents the intrinsic scattering type. β_i is related to the polarimetric orientation angle of the radar line-of-sight (LOS). The probabilistic model gives the polarimetric *H* and $\bar{\alpha}$ as

$$H = -\sum_{i=1}^{3} p_i \log_3(p_i), \quad (5)$$

$$\bar{\alpha} = \sum_{i=1}^{3} p_i \alpha_i, \quad (6)$$

where scattering probabilities are derived by

$$p_i = \frac{\lambda_i}{\sum_{k=1}^{3} \lambda_k} \text{ with } \sum_{k=1}^{3} p_i = 1. \quad (7)$$

H represents the degree of the statistical disorder of each distinct scatter type within the ensemble [12]. The higher *H* indicates high scattering randomness. $\bar{\alpha}$ identifies the dominant scattering mechanism for random media. The three dominant scattering states of $\bar{\alpha}$ are single-bounce scattering ($\bar{\alpha} \to 0$), dipole-like scattering ($\bar{\alpha} \to \pi/4$), and double-bounce scattering or helix scattering ($\bar{\alpha} \to \pi/2$).

A spatial multilooking operation practically realizes ensemble averaging in (1), assuming ergodicity and spatial stationarity of the corresponding samples, because of the lack of temporal polarimetric data stack in spaceborne and airborne SAR. This process generally degrades the spatial resolution and has a risk of mixing different distributions, leading to a biased estimate of the decomposition values [13], [17].

Nonetheless, the above issues can be solved by temporal averaging. The GB-SAR observation, which enables dense temporal monitoring, makes this implementation possible. The stationary observation in GB-SAR monitoring can also fix the incidence angle along the time sequence. This configuration is suited for temporal averaging because the scattering mechanism has the incidence angle dependence [18].

The ensemble-averaged coherency matrix is then realized by temporal averaging, assuming temporal stationarity as

$$\mathbf{T}_{\mathrm{temp}} = \frac{1}{N} \sum_{n}^{N} \mathbf{k}_p^n \mathbf{k}_p^{n*\mathrm{T}}, \quad (8)$$

where *n* is the acquisition time indices and *N* is the number of polarimetric data along time. The temporal averaged coherency matrix is decomposed into eigenvectors and eigenvalues, followed by a derivation of the temporal entropy H_{temp} and temporal mean alpha angle $\bar{\alpha}_{\mathrm{temp}}$ values with (5) and (6). Accordingly, the derived H_{temp} value indicates a descriptor that accounts for the backscattering process's degree of temporal stationarity. $\bar{\alpha}_{\mathrm{temp}}$ value shows a dominant scattering mechanism within the defined time window.

IV. Application to Landslide Monitoring

Through the restoration work period over the postlandslide slope, a small-scale secondary debris flow (hereafter referred to as "landslide") occurred at the middle part of the monitored slope triggered by heavy rain on June 30, 2019. Fig. 3 shows the observed postlandslide mountainous slope and the enlarged view of the landslide. Two regions of interest (ROI) were defined within the landslide affected zone for further processing: ROI-I in the avalanche region and ROI-II in the debris cover region [see Fig. 3(d)]. The land cover in ROI-I and II before the landslide showed mainly sparse vegetated cover [see Fig. 3(a)]. After the landslide occurrence, a part of the vegetation in ROI-I flowed away due to the avalanche. The vegetation in ROI-II was then covered with debris. The landslide's exact occurrence time was unknown because the installed optical camera failed to visualize the landslide due to the dark (pre-dawn morning) and foggy conditions.

A. Processing Chain

The number of samples in the averaging operation affects the polarimetric *H* estimation. As demonstrated in [13] and [17], the bias in *H* was pronounced in the case of the insufficient number of averaging samples, leading to a wrong interpretation of the target character. Therefore, a tradeoff between bias and temporal resolution must be considered according to the system operational mode. In this analysis, the processing chain defined the 1 h temporal averaging window to derive H_{temp} and $\bar{\alpha}_{\mathrm{temp}}$ values. GB-SAR acquired polarimetric images each 5 min; thus, 12 polarimetric data were temporally averaged within 1 h. Sliding this temporal window by 30 min realized the time series of H_{temp} and $\bar{\alpha}_{\mathrm{temp}}$ values. Therefore, the temporal window was slid with overwrapping, providing a smoother time-series outcome.

The polarimetric calibration was preliminarily applied to all the polarimetric data. The Appendix demonstrates the practical polarimetric calibration methodology using the trihedral corner refractor (CR) adopted in this analysis.

B. Properties of $H_{\mathrm{temp}}/\bar{\alpha}_{\mathrm{temp}}$ and $H_{\mathrm{spatial}}/\bar{\alpha}_{\mathrm{spatial}}$ Parameters Over the Observed Terrain

Several types of land cover exist in the observed postlandslide slope. For example, the slope recovery project covered the metal wire mesh over the observed slope's upper part for restoration. The white dashed line represents the spatial coverage of the metal wire mesh, as shown in Fig. 3(a). Understanding the properties of $H_{\mathrm{temp}}/\bar{\alpha}_{\mathrm{temp}}$ and $H_{\mathrm{spatial}}/\bar{\alpha}_{\mathrm{spatial}}$ parameters over such regions is significant for later landslide monitoring.

We address herein an investigation of three land cover types, namely metal wire mesh cover (ROI-W), bare surface terrain (ROI-G), and vegetation cover (ROI-V). In this investigation, the polarimetric data acquired on August 25, 2018, were employed. There was no rainfall on this day. Fig. 4 presents the digital elevation model (DEM) acquired in July 2018, which shows almost the same land cover as August 2018, indicating the selected ROI location. Note that the land cover had changed

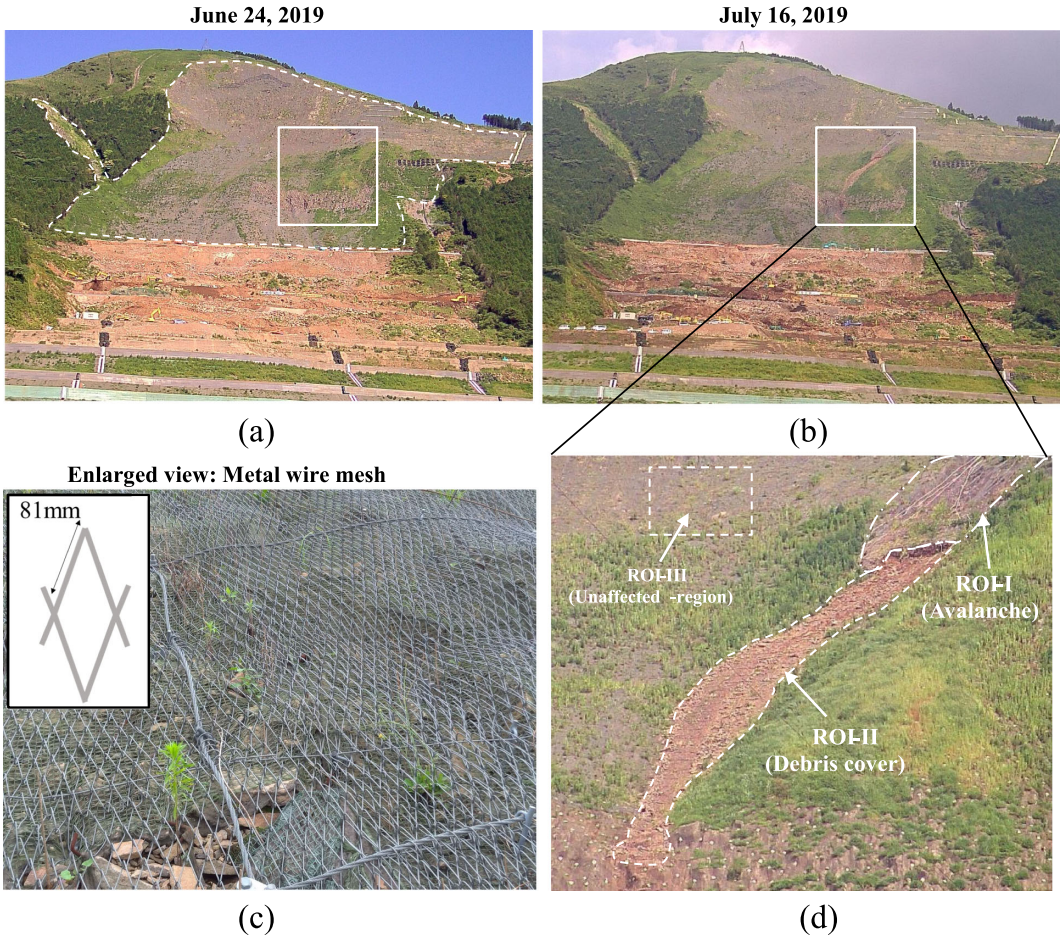

Fig. 3. (a) View of the observed post-landslide mountainous slope before the landslide event (taken on June 24, 2019). The white dashed line indicates the spatial coverage of the metal wire mesh. The white rectangular indicates the location of the landslide. (b) View of the observed post-landslide mountainous slope after the landslide event (taken on June 16, 2019). (b) An enlarged view of the metal wire mesh cover. (c) Landslide caused by the heavy rainfall (occurred on June 30, 2019).

from day to day because of the daily slope reinforcement and earthwork. A comparison of Figs. 3 and 4 showed the increase of the metal wire mesh coverage.

In this analysis, we derived both $H_{\mathrm{temp}}/\bar{\alpha}_{\mathrm{temp}}$ and $H_{\mathrm{spatial}}/\bar{\alpha}_{\mathrm{spatial}}$ values using the 12 polarimetric data acquired from 11:02 A.M. to 11:57 A.M. of August 25, 2018. H_{spatial} and $\bar{\alpha}_{\mathrm{spatial}}$ values were derived by the polarimetric data acquired at 11:57 A.M. with a 4×3 rectangular spatial window to average 12 pixels equivalent to the number of temporal samples in $H_{\mathrm{temp}}/\bar{\alpha}_{\mathrm{temp}}$. Note that the same number of averaging samples kept a fair comparison because the averaging number influenced the bias in the $H/\bar{\alpha}$ parameters, as demonstrated in Section IV-A. Fig. 5 presents the derived decomposition images. Fig. 6 shows distributions of both $H_{\mathrm{temp}}/\bar{\alpha}_{\mathrm{temp}}$ and $H_{\mathrm{spatial}}/\bar{\alpha}_{\mathrm{spatial}}$ over the three ROIs plotted on the $H/\bar{\alpha}$ 2D space. Table I lists the mean decomposition values averaged over each ROI. Nine zones were specified on $H/\bar{\alpha}$ 2D space related to specific scattering characteristics (right side, Fig. 6 [12]). These bounds are based on the scattering mechanism's properties and are not dependent on a particular dataset [19].

TABLE I
ROI-AVERAGED $H_{\mathrm{temp}}/\bar{\alpha}_{\mathrm{temp}}$ AND $H_{\mathrm{spatial}}/\bar{\alpha}_{\mathrm{spatial}}$ VALUES FOR THE SELECTED THREE ROIS.

ROI	H_{temp}	H_{spatial}	$\bar{\alpha}_{\mathrm{temp}}$	$\bar{\alpha}_{\mathrm{spatial}}$
ROI_W	0.32	0.84	49.49	49.02
ROI_G	0.17	0.49	30.00	21.61
ROI_V	0.75	0.76	40.04	39.85

Although the ground-truth of the investigated vegetation and the terrain surface morphology was not available, the analysis was made to perform a comparative evaluation of the ROIs and between two methods for later landslide monitoring. Consequently, the performed analysis reveals different $H/\bar{\alpha}$ results between temporal and spatial averaging. In the following, we provide the interpretation of the decomposition results for each ROI.

1) ROI-W: Similar ROI-averaged values between $\bar{\alpha}_{\mathrm{temp}}$ and $\bar{\alpha}_{\mathrm{spatial}}$ were found for ROI-W ($\bar{\alpha}_{\mathrm{temp}} = 49.49°$, $\bar{\alpha}_{\mathrm{spatial}} = 49.02°$ in Table I). These values corresponded to the dipole-like scattering mechanism. The results revealed that the metal wire

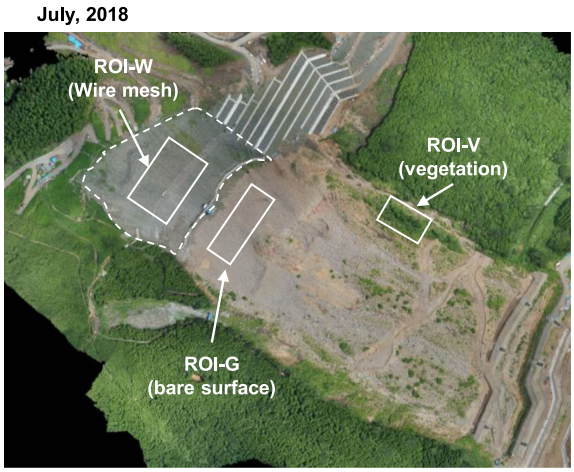

Fig. 4. DEM observed in July, 2018. The white rectangular indicates the investigated ROIs. The white dashed line indicates the spatial coverage of the metal wire mesh in July, 2018.

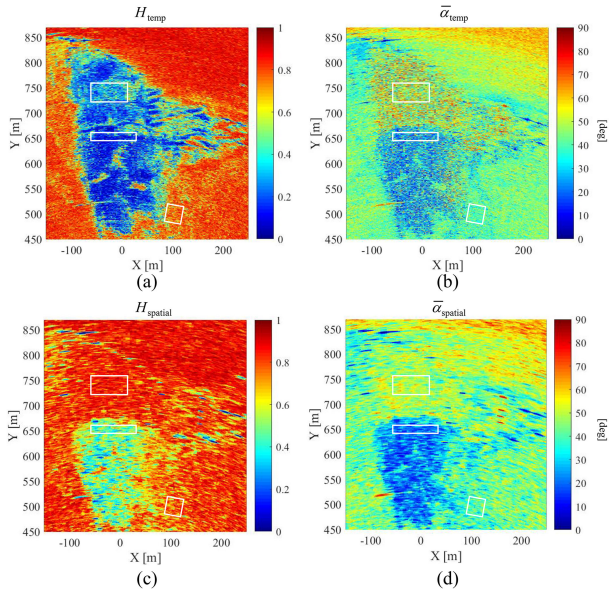

Fig. 5. Decomposition results of $H_{\mathrm{temp}}/\bar{\alpha}_{\mathrm{temp}}$ and $H_{\mathrm{spatial}}/\bar{\alpha}_{\mathrm{spatial}}$. The results of H_{temp} and $\bar{\alpha}_{\mathrm{temp}}$ are derived by the polarimetric data acquired from 11:02 A.M. to 11:57 A.M. August 25, 2018. The results of H_{spatial} and $\bar{\alpha}_{\mathrm{spatial}}$ are derived by the polarimetric data acquired at 11:57 A.M. of August 25, 2018. (a) H_{temp}. (b) $\bar{\alpha}_{\mathrm{temp}}$. (c) H_{spatial}. (d) $\bar{\alpha}_{\mathrm{spatial}}$. The white rectangular symbol indicates the investigated ROIs.

mesh produced a dipole-like scattering in Ku-band. This was plausible because the length of one side of the wire mesh is ≈81 mm, which is 4.7 times longer than the Ku-band wavelength (17.4 mm) with a wire thickness of 3.2 mm in diameter [see Fig. 3(c)]. Therefore, metal wire mesh can be assumed to be modeled by a cloud of a randomly oriented dipole-like object in the Ku-band plotted on zone-8 or zone-5 of $H/\bar{\alpha}$ 2D space. Furthermore, $\bar{\alpha}_{\mathrm{temp}}$ values in ROI-W had a wider distribution than $\bar{\alpha}_{\mathrm{spatial}}$ and $\bar{\alpha}_{\mathrm{temp}}$ of the other two regions [see Fig. 6(a)]. This indicated the existence of a variety of scattering mechanisms over ROI-W, varying pixel-to-pixel. On the contrary, a large difference of 0.52 was observed between the ROI-averaged H_{temp} and H_{spatial} ($H_{\mathrm{temp}} = 0.32$, $H_{\mathrm{spatial}} = 0.84$ in Table I). The spatial multilooking of heterogeneous pixels caused the higher H_{spatial} in terms of the scattering mechanism [4], [13], which is understood by the broader distribution of $\bar{\alpha}_{\mathrm{temp}}$. Meanwhile, a lower H_{temp} value revealed the stable variation of the polarimetric response along the temporal axis.

2) ROI-G: The decomposition parameters from ROI-G revealed low $\bar{\alpha}_{\mathrm{temp}}$ and $\bar{\alpha}_{\mathrm{spatial}}$ results (ROI-averaged $\bar{\alpha}_{\mathrm{temp}} = 30°$ and $\bar{\alpha}_{\mathrm{spatial}} = 21°$), indicating the surface scattering mechanism typically presented over the bare surface terrain. The $\bar{\alpha}_{\mathrm{temp}}$ distribution was wider than that of $\bar{\alpha}_{\mathrm{spatial}}$, which might be explained by the spatial variation of the terrain surface morphology. In contrast, H_{spatial} results appeared higher than H_{spatial} values, and half of $H_{\mathrm{spatial}}/\bar{\alpha}_{\mathrm{spatial}}$ plots were located on zone-6, which corresponded to the medium entropy surface scattering in Fig. 6(e). The spatial averaging again influenced the increased H values over the terrain due to the variety of scattering mechanisms revealed by $\bar{\alpha}_{\mathrm{temp}}$ distribution.

3) ROI-V: Unlike ROI-W and ROI-G, ROI-V showed a similar distribution between $H_{\mathrm{temp}}/\bar{\alpha}_{\mathrm{temp}}$ and $H_{\mathrm{spatial}}/\bar{\alpha}_{\mathrm{spatial}}$ on the 2-D space. Both distributions were located around zone-5, which corresponded to medium entropy vegetation scattering. H_{temp} over ROI-V depicted the highest values among H_{temp} values of the three ROIs, which was likely caused by the wind-driven vegetation temporal fluctuation. The medium H_{spatial} (ROI-averaged $H_{\mathrm{spatial}} = 0.76$) over the ROI-V resulted from the spatial multilooking of random media (heterogeneous pixels).

C. Influence of Rainfall in $H_{\mathrm{temp}}/\bar{\alpha}_{\mathrm{temp}}$ Decomposition

The propagation delay caused by rainfall along a propagation path affects the polarimetric data [20], [21]. Rainfall causes a polarization-dependent phase shift through the propagation in the medium, which leads to the copolarization phase difference (CPD). Polarization-dependent signal attenuation and cross-pol interference may also appear. The rain polarization effects mainly occur due to the spheroid shape raindrops driven by gravity and the raindrop alignment (canting angle) [22]. Hence, such parameters on the anisotropic raindrop shape, raindrop size distributions, and raindrop's orientation angle along the propagation path determine co-pol phase shift and attenuation. Heavy rain over a propagation path will severely limit measurement reliability. Therefore, a proper understanding of the rainfall effect in the measured GB-SAR backscattering data is significant.

An 11-day time series of a trihedral CR response was measured and plotted in Fig. 7 to assess rainfall's influence on the polarimetric dataset. Fig. 8 depicts the employed trihedral CR. Fig. 7(a) shows the rainfall rate measured at the observed area by the installed weather sensor. Fig. 7(b) and (c) illustrate the copolarization channel imbalance of the phase and the amplitude measured at a single pixel corresponding to the CR. Fig. 7(d) and (e) show H_{temp} and $\bar{\alpha}_{\mathrm{temp}}$ values derived by the processing chain demonstrated in Section IV-A. At a glance, the channel imbalances of the phase and the amplitude correlated well with

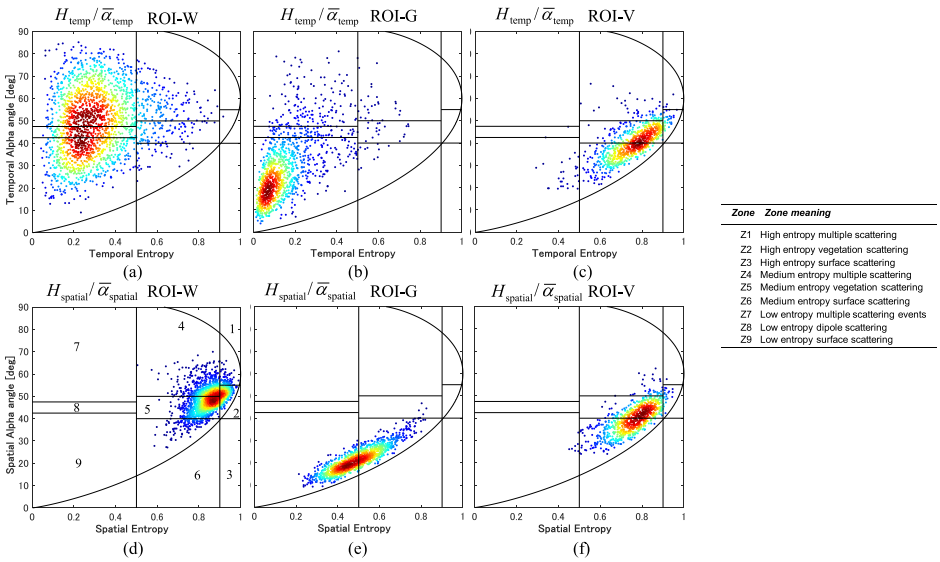

Fig. 6. (a)–(c) $H_{\mathrm{temp}}/\bar{\alpha}_{\mathrm{temp}}$ distributions for the ROI-W, ROI-G, and ROI-V on the 2-D space. (d)–(f) $H_{\mathrm{spatial}}/\bar{\alpha}_{\mathrm{spatial}}$ distributions. The color represents the density of plots. Nine zones are specified in (d). The corresponding scattering characteristics are described at the right side.

the rainfall rate and indicated the same peak time. The CPD and the amplitude ratio reached ≈38° and −4.9 dB, respectively, at the peak time. Accordingly, the copolarization channel imbalance affected the polarimetric decomposition results. Both H_{temp} and $\bar{\alpha}_{\mathrm{temp}}$ results increased as rainfall began, where both increased up to 0.07° and 13.54° in the peak time. We also confirmed that H_{temp} time series' peak time (5:30 A.M. June 30) was almost in accordance with the rainfall rate's peak time (6:00 A.M. June 30).

The backscattering from natural terrains, such as soil surface and vegetation, contains an additional rainfall effect when the dielectric constant (moisture) and roughness over the terrain surface turn into change. These surface parameter changes modify the scattering matrix and the polarimetric decomposition parameters. The dielectric constant is one of the parameters modifying the copolarization amplitude imbalance, while the surface roughness increases the cross-polarization term [23]. A H_{temp} simulation demonstrated in [3] revealed that if the copolarization amplitude imbalance becomes 3 dB without any phase difference, H_{temp} reaches nearly 0.1 in the worst case.

According to the abovementioned facts, multiple sources of rainfall effects must be considered depending on the terrain situations. Such effects lead to a difficult polarimetric data interpretation because the separation of rainfall effects and the actual terrain surface change (i.e., change induced by a landslide) is challenging. To separate both phenomena as much as possible, we also analyze the time-series data of a CR and the region unaffected by a landslide.

D. Landslide Monitoring

1) $H_{\mathrm{temp}}/\bar{\alpha}_{\mathrm{temp}}$ Results: Fig. 9(a) and (b) displays six days of $H_{\mathrm{temp}}/\bar{\alpha}_{\mathrm{temp}}$ time series from June 26 until July 1, 2019. The time-series results were derived by the corresponding subset of polarimetric images acquired within 1 h (e.g., the result at 0:00 A.M. was estimated by the data observed from 0:00 A.M. to 1:00 A.M.) and averaged over each ROI. The light gray shading indicates the expected landslide occurrence time on June 30, 2019, in (see Fig. 9). In addition to two defined regions (i.e., ROI-I and ROI-II), the time series of the region unaffected by the landslide is also plotted in Fig. 9 and denoted as ROI-III. The land cover in ROI-III included both metal wire mesh and sparse vegetation. Fig. 3(d) depicts the ROI-III location.

Fig. 9(a) shows the gap (≈0.2) of H_{temp} time series between the landslide regions (ROI-I and II) and ROI-III before June 30. This gap indicates different temporal backscattering characteristics within a time-window. Nonetheless, H_{temp} time series of all ROIs showed similar trends. During rainfall, H_{temp} values in three ROIs illustrated an upward trend from 26th to 30th with a ≈0.2 increase. The result of ROI-I reached a peak at 3:30 A.M.; the other regions reached a peak at 5:00 A.M.

After the peak, H_{temp} time series started to decrease until the end of investigation time with significant fluctuations. Consequently, the gap between the landslide regions (ROI-I and II) and ROI-III became smaller.

In Fig. 9(b), all ROIs revealed $\bar{\alpha}_{\mathrm{temp}}$ values close to 45°, which corresponded to a dipole-like scattering before June 30 because of the wire mesh cover and vegetation. The ROI-I revealed a scattering mechanism transition at around 3:30 A.M. of June 30, while ROI-II revealed one at around 2:00 A.M. of June 30. From the transition time, $\bar{\alpha}_{\mathrm{temp}}$ time series in ROI-I showed a gentle upward trend with a 4.29° increase (from 1:00 A.M. to 1:00 P.M. of June 30), while that of ROI-II significantly dropped with an 8.96° decrease. On the contrary, ROI-III showed no major change (only a 1.38° increase was observed from 1:00 A.M. to 1:00 P.M. on June 30).

Fig. 10(a)–(d) depicts H_{temp} and $\bar{\alpha}_{\mathrm{temp}}$ images before (8:00 P.M. of June 29) and after (11:00 A.M. of June 30) the landslide event. The black dashed lines in Fig. 10 indicate the ROI-I, ROI-II, and ROI-III locations. The visual changes of H_{temp} and

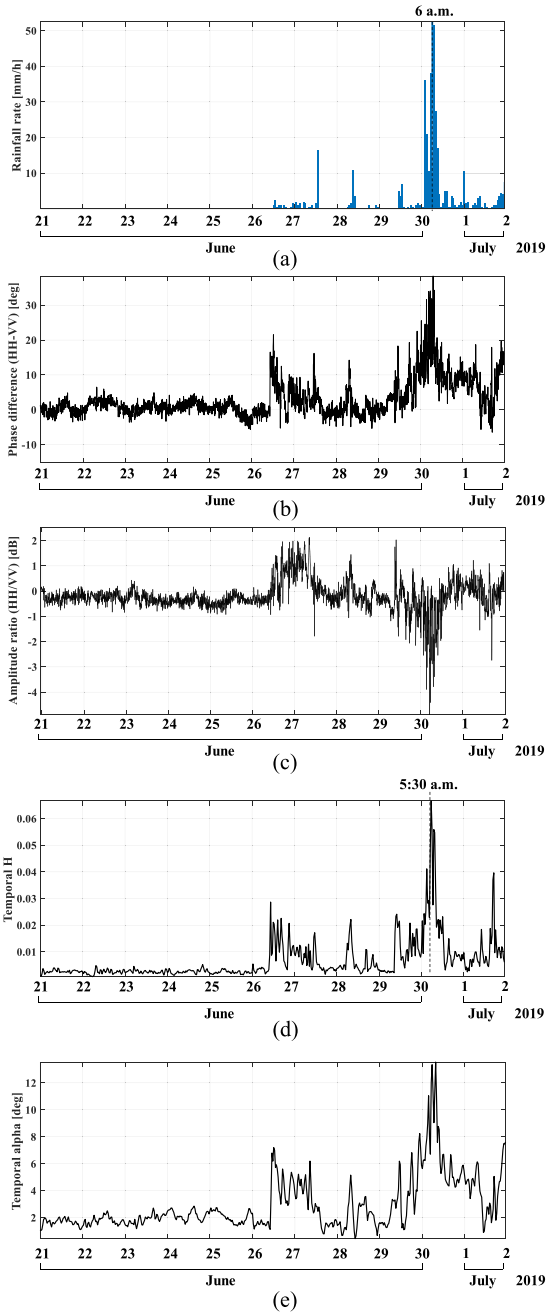

Fig. 7. Polarimetric response of the trihedral CR. (a) Rainfall rate measured by the weather sensor at the observed slope. (b) Copolarization phase difference. (c) Copolarization amplitude ratio. (d) H_{temp}. (e) $\bar{\alpha}_{\mathrm{temp}}$.

$\bar{\alpha}_{\mathrm{temp}}$ were apparent over ROI-II before and after the landslide, as shown in Fig. 10(a)–(d). Note that the high H_{temp} region, appearing from 600 to 650 of a slant range corresponded to the vegetation cover, as confirmed by Fig. 3(b). The wind-driven vegetation temporal fluctuation caused high H_{temp}, demonstrated in Section IV-B.

The hourly values in Fig. 9(a) and (b) are plotted on the 2-D $H/\bar{\alpha}$ space to jointly describe the temporal transition of H_{temp} and $\bar{\alpha}_{\mathrm{temp}}$ values, as presented in Figs. 11(a) and (b). The plot color represents the observation time from June 26 to July 1, 2019. A total of 144 $H_{\mathrm{temp}}/\bar{\alpha}_{\mathrm{temp}}$ plots are drawn in Fig. 11.

Fig. 8. One of the installed trihedral CRs at the observed slope.

Both ROI-I and II showed the temporal transition from zone-8 to zone-5 before the landslide due to the rainfall. After the landslide, the plots on ROI-I moved toward zone-7, while those of ROI-II moved toward zone-9.

2) $H_{\mathrm{spatial}}/\bar{\alpha}_{\mathrm{spatial}}$ Results: Six days of landslide transition were investigated using $H_{\mathrm{spatial}}/\bar{\alpha}_{\mathrm{spatial}}$ parameters in the three ROIs. Fig. 9(c) and (d) displays H_{spatial} and $\bar{\alpha}_{\mathrm{spatial}}$ time series from June 26 until July 1, 2019. A $4\times$ 3 rectangular spatial window was used for the multilooking in $H_{\mathrm{spatial}}/\bar{\alpha}_{\mathrm{spatial}}$ to average 12 pixels. Fully polarimetric data every 30 min were used to derive the time series in Fig. 9(c) and (d).

The H_{spatial} time-series results of the three ROIs appeared higher than H_{temp} values. Before June 30, ROI-II and ROI-III showed similar H_{spatial} values ($H_{\mathrm{spatial}} \approx 0.81$), while ROI-I depicted a higher H_{spatial} than the other ROIs ($H_{\mathrm{spatial}} \approx 0.84$). Slight H_{spatial} transitions are shown in Fig. 9(c). From 1:00 A.M. to 1:00 P.M. of June 30, H_{spatial} time series of ROI-I showed an upward trend with a 0.02 increase, whereas ROI-II showed a downward trend with a 0.05 decrease. The ROI-III also exhibited a slight upward trend with a 0.04 increase from 1:00 A.M. to 1:00 P.M.

The $\bar{\alpha}_{\mathrm{spatial}}$ time-series results over ROI-I and ROII were similar to those of $\bar{\alpha}_{\mathrm{temp}}$ time series. The ROI-I revealed scattering mechanism transition at around 3:30 A.M. of June 30, while ROI-II revealed one at around 2:00 A.M. of June 30. From the transition time, $\bar{\alpha}_{\mathrm{spatial}}$ time series in ROI-I showed an upward trend with a 2.3° increase (from 1:00 A.M. to 1:00 P.M. of June 30), while that of ROI-II dropped with a 2.79° decrease. ROI-III showed a 2.06° increase from 1:00 A.M. to 1:00 P.M. on June 30. The amount of $\bar{\alpha}_{\mathrm{spatial}}$ change in ROI-II was smaller than that of $\bar{\alpha}_{\mathrm{temp}}$, whereas ROI-I presented a comparable amount of change between $\bar{\alpha}_{\mathrm{temp}}$ and $\bar{\alpha}_{\mathrm{spatial}}$ time series.

Fig. 10(e)–(h) shows the processed H_{spatial} and $\bar{\alpha}_{\mathrm{spatial}}$ images observed at 8:00 P.M. of June 29 and 11:00 A.M. of June 30 [similar observation time as in Fig. 10(a)–(d)], showing the derived images before and after the landslide. At a glance, visual H_{spatial} and $\bar{\alpha}_{\mathrm{spatial}}$ changes were hardly seen from the comparison images over the landslide region. H_{spatial} results

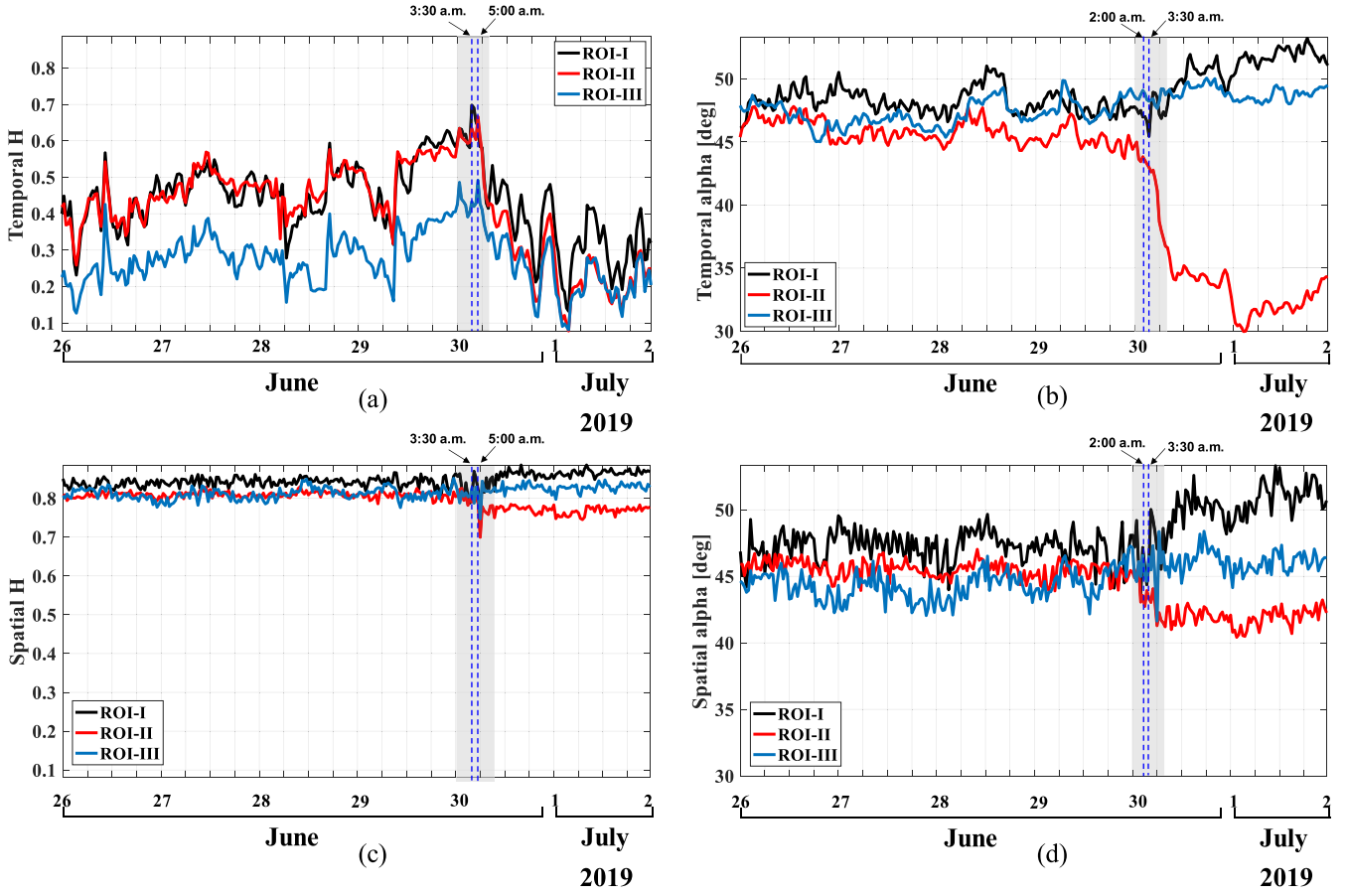

Fig. 9. Time series of $H_{\mathrm{temp}}/\bar{\alpha}_{\mathrm{temp}}$ and $H_{\mathrm{spatial}}/\bar{\alpha}_{\mathrm{spatial}}$ results derived for each 30 min in ROI-I (black plot), ROI-II (red plot), and ROI-III (blue plot). (a) H_{temp}. (b) $\bar{\alpha}_{\mathrm{temp}}$. (c) H_{spatial}. (d) $\bar{\alpha}_{\mathrm{spatial}}$.

higher than H_{temp} images can be confirmed over the upper part of the slope due to the metal wire mesh cover.

The temporal transition of $H_{\mathrm{spatial}}/\bar{\alpha}_{\mathrm{spatial}}$ time series was plotted on the 2-D space in Fig. 11(c) and (d). Although slight $H_{\mathrm{spatial}}/\bar{\alpha}_{\mathrm{spatial}}$ transitions were confirmed in both ROI-I and ROI-II, most of the plots remained in zone-5, which corresponded to medium entropy vegetation scattering. After the landslide, the plots on ROI-I moved toward zone-4, while those on ROI-II moved toward zone-6.

V. Discussion

This section presents an interpretation of $H_{\mathrm{temp}}/\bar{\alpha}_{\mathrm{temp}}$time-series results in the previous section concerning the landslide event. The applicability of $H_{\mathrm{temp}}/\bar{\alpha}_{\mathrm{temp}}$ target decomposition parameters is also discussed by comparing it with that of the $H_{\mathrm{spatial}}/\bar{\alpha}_{\mathrm{spatial}}$ results.

A. Interpretation

Rainfall makes the interpretation difficult; hence, CR and ROI-III were analyzed. Here, the time-series fluctuations of the $H_{\mathrm{temp}}/\bar{\alpha}_{\mathrm{temp}}$ results in ROI-III were assumed to be caused only by the rainfall effect through the propagation and rainfall-driven soil-moisture and surface roughness changes.

According to the time series of H_{temp} in the three ROIs and the CR, H_{temp} time series' peak time in ROI-I was 1.5 h earlier than the other two regions and 2 h earlier than the CR. Only ROI-I showed an abrupt H_{temp} increase of 0.12 from 3:00 A.M. ($H_{\mathrm{temp}} = 0.58$) to 3:30 A.M. ($H_{\mathrm{temp}} = 0.70$), while ROI-II, ROI-III, and CR showed slight H_{temp} changes of 0.03, 0.03, and 0.01, respectively. Therefore, the abrupt increase of H_{temp} in ROI-I can be assumed to be caused by the landslide because the CR and ROI-III revealed fewer rainfall effects (small changes of H_{temp}) at the same time. The $\bar{\alpha}_{\mathrm{temp}}$ time-series results supported this assumption where those of ROI-I and ROI-II revealed the changes of the temporal trend. The $\bar{\alpha}_{\mathrm{temp}}$ time series in ROI-I started to increase from 3:30 A.M. In contrast, ROI-II showed a decrease from 2:00 A.M. From the ROI-II results, we expect that debris flowing over ROI-II started around 2:00 A.M. On the contrary, the main avalanche in ROI-I was expected to occur around 3:30 A.M. because both H_{temp} and $\bar{\alpha}_{\mathrm{temp}}$ in ROI-I changed at this time.

Fig. 9(b) reveals that ROI-I and ROI-II have different temporal transitions of the scattering mechanisms after the landslide. According to Fig. 11(a), $H_{\mathrm{temp}}/\bar{\alpha}_{\mathrm{temp}}$ in ROI-I are plotted on

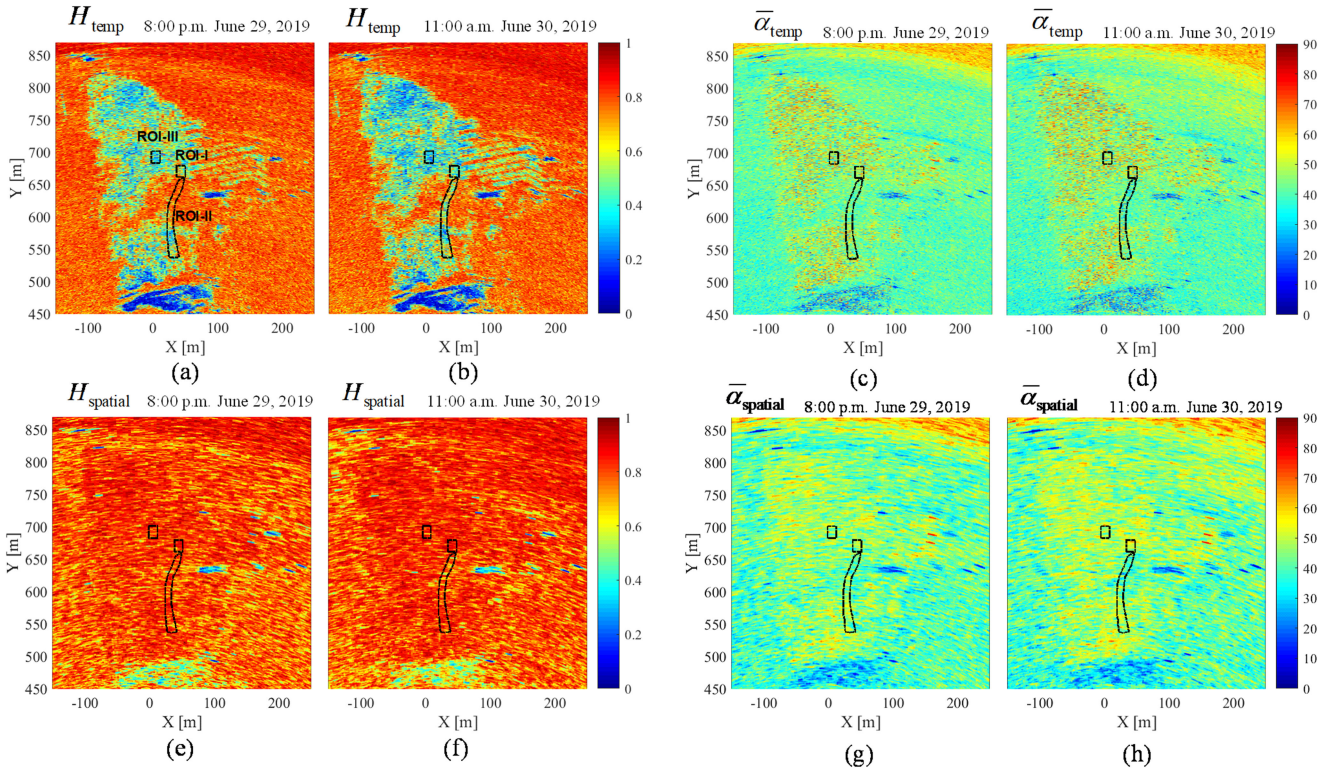

Fig. 10. $H_{\text{temp}}/\bar{\alpha}_{\text{temp}}$ and $H_{\text{spatial}}/\bar{\alpha}_{\text{spatial}}$ images derived at 8:00 P.M. June 29, 2019 and 11:00 A.M. June 30, 2019. Black dashed lines indicate the ROI-I, ROI-II, and ROI-III, respectively, where each location can be given in (a). (a), (c), (e), (g) Images derived at 8:00 P.M. June 29, 2019. (b), (d), (f), (h) Images derived at 8:00 P.M. June 29, 2019. (a), (b) H_{temp}. (c), (d) $\bar{\alpha}_{\text{temp}}$. (e), (f) H_{spatial}. (g), (h) $\bar{\alpha}_{\text{spatial}}$.

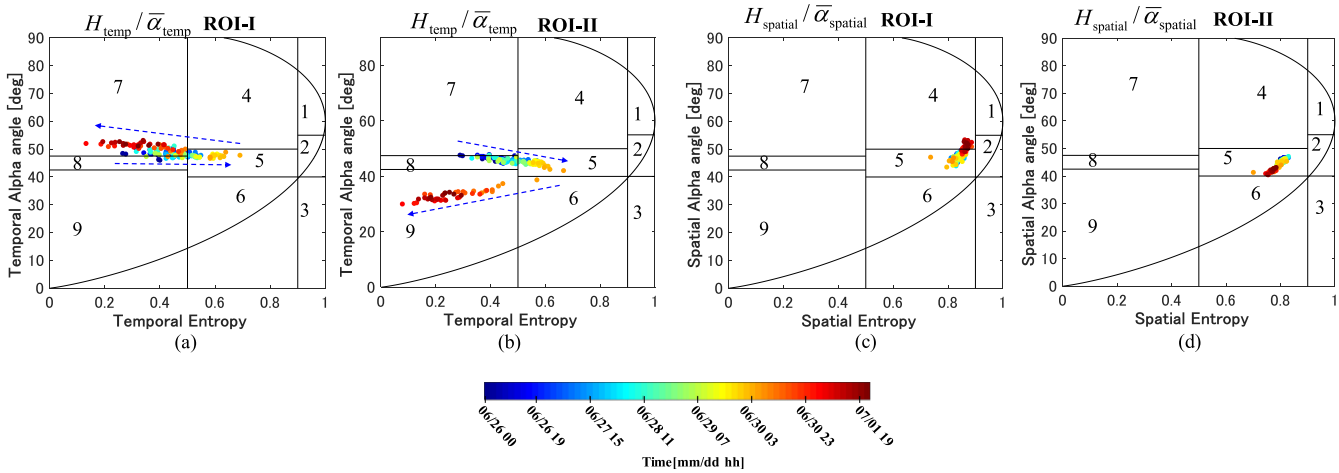

Fig. 11. Temporal transition of the hourly $H/\bar{\alpha}$ results of the ROI-I and ROI-II on the 2-D space. Plot color represents observation time from 0:00 A.M. June 26 to 11:59 P.M. July 1, 2019. In total 144 plots are drawn in each figure. (a) $H_{\text{temp}}/\bar{\alpha}_{\text{temp}}$ plots in the ROI-I. (b) $H_{\text{temp}}/\bar{\alpha}_{\text{temp}}$ plots in the ROI-II. (c) $H_{\text{spatial}}/\bar{\alpha}_{\text{spatial}}$ plots in the ROI-I. (d) $H_{\text{spatial}}/\bar{\alpha}_{\text{spatial}}$ plots in the ROI-II.

zone-7, which corresponds to multiple-scattering events after the landslide. The rupture surface can be expected to cause such scattering events after the loss of mass due to the avalanche in ROI-I. On the contrary, ROI-II indicated the surface scattering mechanism after the landslide caused by the debris accumulation over the ROI-II.

B. Comparison Between $H_{\text{temp}}/\bar{\alpha}_{\text{temp}}$ and $H_{\text{spatial}}/\bar{\alpha}_{\text{spatial}}$

H_{temp} deals with the temporal stationarity of the scattering mechanism; thus, it is only sensitive to temporal scattering variation. Accordingly, H_{temp} becomes an index of the temporal scattering mechanism change. This H_{temp} property is especially appropriate to change detection of the corresponding

scatterers. Meanwhile, H_{spatial} reflects the spatial variation of the scattering mechanism. Therefore, temporal change detection by H_{spatial} deals with the temporal difference of H_{spatial}. If H_{spatial} values are similar before and after the scatterer change, change detection by H_{spatial} becomes challenging. This information difference of H_{temp} and H_{spatial} leads to quite different time-series results between Fig. 9(a) and (c).

Importantly, $H_{\mathrm{temp}}/\bar{\alpha}_{\mathrm{temp}}$ can attain the full spatial resolution without any spatial averaging or mixing. When the scattering mechanism changes pixel-to-pixel, such as the presented Ku-band dataset, spatial averaging causes the mixing of heterogeneous pixels, which increases H_{spatial} values [24]. The mixing of different distributions potentially leads to a wrong interpretation of the nature of scatterers and less spatial contrast (or, in other words, remove the spatial signature). Hence, the smaller decrease of $\bar{\alpha}_{\mathrm{spatial}}$ compared to $\bar{\alpha}_{\mathrm{temp}}$ over ROI-II after the landslide can be explained by the mixing of the debris cover pixels and the neighboring vegetation pixels. In this case, $\bar{\alpha}_{\mathrm{spatial}}$ deals with the contributions of both surface and volume scattering while $\bar{\alpha}_{\mathrm{temp}}$ measures only surface scattering. In addition, the high H_{spatial} increases the inability to distinguish between the scattering mechanisms because a feasible range of $\bar{\alpha}$ gets smaller when the underlying H increases [19].

The $H_{\mathrm{temp}}/\bar{\alpha}_{\mathrm{temp}}$ decomposition sacrifices temporal resolution. Nevertheless, such a drawback can be practically solved by increasing the data acquisition rate, which GB-SAR easily realizes.

VI. Conclusion

We applied herein the temporal $H/\bar{\alpha}$ decomposition approach to landslide monitoring as a GB-SAR continuous data analysis. We employed the dataset observed in the framework of a near-real-time polarimetric GB-SAR monitoring campaign in Minami-Aso, Kumamoto, Japan.

First, the properties of $H_{\mathrm{temp}}/\bar{\alpha}_{\mathrm{temp}}$ and $H_{\mathrm{spatial}}/\bar{\alpha}_{\mathrm{spatial}}$ parameters on the selected regions were investigated. We selected three land cover types over the observed slope, that are metal wire mesh cover (ROI-W), bare surface terrain (ROI-G), and vegetation cover (ROI-G). The $\bar{\alpha}_{\mathrm{temp}}$ results revealed a broader distribution than $\bar{\alpha}_{\mathrm{spatial}}$, especially for ROI-W and ROI-G. These broader $\bar{\alpha}_{\mathrm{temp}}$ results indicated a high scattering spatial diversity. ROI-W and ROI-G showed low H_{temp}, indicating the scattering mechanism's temporal stationarity and a high H_{spatial} caused by the spatial multilooking of heterogeneous pixels. In contrast, the ROI-V showed a similar distribution between $H_{\mathrm{temp}}/\bar{\alpha}_{\mathrm{temp}}$ and $H_{\mathrm{spatial}}/\bar{\alpha}_{\mathrm{spatial}}$ on the 2-D space.

For a better interpretation of $H_{\mathrm{temp}}/\bar{\alpha}_{\mathrm{temp}}$ in the GB-SAR dataset, the impact of rainfall on the polarimetric parameters was investigated using the acquired time-series data. The trihedral CR polarimetric response during rainfall revealed the copolarization phase difference and the polarization-dependent signal attenuation. Accordingly, the derived H_{temp} and $\bar{\alpha}_{\mathrm{temp}}$ parameters were correlated with the rainfall rate, indicating a significant impact of the rainfall effect on the decomposition results.

Triggered by the heavy rain, a small-scale landslide occurred over the observed post-landslide slope on June 30, 2019. The time series $H_{\mathrm{temp}}/\bar{\alpha}_{\mathrm{temp}}$ parameters were analyzed to investigate the feasibility of the detection and temporal scattering mechanism transition over the landslide regions. Three regions were investigated, namely ROI-I in the avalanche region (upper part of landslide), ROI-II in the debris cover region (middle and lower part of landslide), and ROI-III in the region unaffected by the landslide.

The time-series analysis of $H_{\mathrm{temp}}/\bar{\alpha}_{\mathrm{temp}}$ over ROI-I revealed a gentle increase of $\bar{\alpha}_{\mathrm{temp}}$ and an abrupt increase of H_{temp} presumably caused by the avalanche. ROI-II also showed a clear temporal transition of $\bar{\alpha}_{\mathrm{temp}}$ because of the debris cover after the landslide.

Furthermore, $H_{\mathrm{temp}}/\bar{\alpha}_{\mathrm{temp}}$ target decomposition parameters' applicability was discussed by comparing it with the classical $H_{\mathrm{spatial}}/\bar{\alpha}_{\mathrm{spatial}}$ parameters. In summary, the following are the characteristics of temporal averaging compared to spatial averaging supported by the time-series results:

1) The H_{temp} parameter can be an index of the temporal scattering mechanism change. This H_{temp} property is especially appropriate to the change detection of the corresponding scatterers.
2) A full spatial resolution can be attained. Hence, temporal averaging can avoid the spatial mixing of heterogeneous pixels, which causes an increase of H and the mixing of the polarimetric information.

In particular, GB-SAR can receive the abovementioned benefits because many polarimetric data are available in its monitoring with a fixed position. This is a great advantage compared to spaceborne SAR. Although the InSAR technique's displacement estimate is a major objective in GB-SAR campaigns so far, $H_{\mathrm{temp}}/\bar{\alpha}_{\mathrm{temp}}$ parameters can give us additional key information regarding when and how the terrain surface has changed, as demonstrated in our analysis.

Appendix

Polarimetric Calibration

Polarimetric calibration is an important step that is required to derive reliable polarimetric parameters. The system model is defined as follows using the transmitter and receiver distortion matrices $[\mathbf{T}]$ and $[\mathbf{R}]$

$$[\mathbf{M}] = [\mathbf{R}] \cdot [\mathbf{S}] \cdot [\mathbf{T}], \tag{9}$$

where $[\mathbf{M}]$ and $[\mathbf{S}]$ are the measured and desired scattering matrices, respectively. Neglecting the channel imbalance between HV and VH (cross-pol) and assuming reciprocity for the quasi-monostatic radar system, we can simplify the distortion matrices as [25], [26]

$$\begin{bmatrix} M_{\mathrm{HH}} & M_{\mathrm{HV}} \\ M_{\mathrm{VH}} & M_{\mathrm{VH}} \end{bmatrix} = \begin{bmatrix} 1 & \delta_y \\ \delta_x & f \end{bmatrix} \cdot \begin{bmatrix} S_{\mathrm{HH}} & S_{\mathrm{HV}} \\ S_{\mathrm{VH}} & S_{\mathrm{VH}} \end{bmatrix} \cdot \begin{bmatrix} 1 & \delta_x \\ \delta_y & f \end{bmatrix}, \tag{10}$$

where δ_x and δ_y account for the cross-talk of the horizontal and vertical polarizations, respectively, f represents a channel

imbalance (amplitude and phase) between the HH and VV components (co-pol), and S_{rt} indicates the transmitted polarization (t), and received polarization (r).

According to the 24 h outdoor experiment on a clear weather day, the time-series CR response revealed a very low amplitude ratio of cross-pol to co-pol lower than -30 dB. Therefore, the cross-talk calibration was also not considered herein due to the employed GB-SAR system's good polarization isolation capability. Consequently, the system model in (10) can be further simplified to

$$\begin{bmatrix} M_{\mathrm{HH}} & M_{\mathrm{HV}} \\ M_{\mathrm{VH}} & M_{\mathrm{VH}} \end{bmatrix} = \begin{bmatrix} 1 & 0 \\ 0 & f \end{bmatrix} \cdot \begin{bmatrix} S_{\mathrm{HH}} & S_{\mathrm{HV}} \\ S_{\mathrm{VH}} & S_{\mathrm{VH}} \end{bmatrix} \cdot \begin{bmatrix} 1 & 0 \\ 0 & f \end{bmatrix}, \quad (11)$$

and we obtain the following relationship [27]:

$$\frac{M^*_{\mathrm{VV}} M_{\mathrm{VV}}}{M^*_{\mathrm{HH}} M_{\mathrm{HH}}} = |f|^4 \frac{S^*_{\mathrm{VV}} S_{\mathrm{VV}}}{S^*_{\mathrm{HH}} S_{\mathrm{HH}}}. \quad (12)$$

The point-target copolarization reflector response enables the channel imbalance f computation. The use of a trihedral CR response is appropriate for this purpose because it shows a higher radar cross-section (RCS) and a smaller incidence angle dependence than other canonical targets. The trihedral CR of the desired scattering matrix is generally assumed as

$$[S]_{\mathrm{tri}} = \begin{bmatrix} 1 & 0 \\ 0 & 1 \end{bmatrix}. \quad (13)$$

Therefore, f is computed as

$$|f| = \left(\frac{M^*_{\mathrm{VV}} M_{\mathrm{VV}}}{M^*_{\mathrm{HH}} M_{\mathrm{HH}}} \right)^{\frac{1}{4}}, \quad (14)$$

$$\arg(f) = \frac{1}{2} \arg\left(M^*_{\mathrm{HH}} M_{\mathrm{VV}} \right), \quad (15)$$

where $[\mathbf{M}]$ can be obtained by the temporal mean value of several days of trihedral CR response.

The GB-SAR system is generally calibrated in the field appropriate for radar calibration, such as an electromagnetic (EM) anechoic chamber and a vast field without any object before installation on the monitoring site. In our case, the on-site calibration strategy is conducted, accepting practical polarimetric calibration solutions in the GB-SAR continuous operational mode. Several trihedral CRs are installed over the observed slope, as shown in Fig. 8. The presented polarimetric calibration employs the response from one of the trihedral CRs showing the best copolarization imbalance and cross-talk for the matrix $[\mathbf{M}]$. We must use the response of the CRs acquired under good weather conditions because precipitation significantly affects the signal attenuation and the polarimetric response through the propagation path.

ACKNOWLEDGMENT

The author would like to thank the Ministry of Land, Infrastructure, Transport and Tourism Kyushu Regional Development Bureau and Kumagai Gumi for their support in the field site and for providing them with local information and DEM data.

REFERENCES

[1] D. Tarchi, E. Ohlmer, and A. Sieber, "Monitoring of structural changes by radar interferometry," *Res. Nondestruct. Eval.*, vol. 9, no. 4, pp. 213–225, 1997.
[2] M. Pieraccini and L. Miccinesi, "Ground-based radar interferometry: A bibliographic review," *Remote Sens,* vol. 11, no. 9, 2019, Art. no. 1029.
[3] L. Pipia, X. Fabregas, A. Aguasca, and C. Lopez-Martinez, "Polarimetric temporal analysis of urban environments with a ground-based SAR," *IEEE Trans. Geosci. Remote Sens.*, vol. 51, no. 4, pp. 2343–2360, Apr. 2013.
[4] S. Baffelli, O. Frey, and I. Hajnsek, "Polarimetric analysis of natural terrain observed with a ku-band terrestrial radar," *IEEE J. Sel. Topics Appl. Earth Observ. Remote Sens.*, vol. 12, no. 12, pp. 5268–5288, Dec. 2019.
[5] Z. S. Zhou, W. M. Boerner, and M. Sato, "Development of a ground-based polarimetric broadband SAR system for noninvasive ground-truth validation in vegetation monitoring," *IEEE Trans. Geosci. Remote Sens.*, vol. 42, no. 9, pp. 1803–1810, Sep. 2004.
[6] Y. Izumi, S. Demirci, M. Z. bin Baharuddin, T. Watanabe, and J. T. S. Sumantyo, "Analysis of dual- and full-circular polarimetric SAR modes for rice phenology monitoring: An experimental investigation through ground-based measurements," *Appl. Sci.*, vol. 7, no. 4, 2017, Art. no. 368.
[7] R. Iglesias, D. Monells, X. Fabregas, J. J. Mallorqui, A. Aguasca, and C. Lopez-Martinez, "Phase quality optimization in polarimetric differential SAR interferometry," *IEEE Trans. Geosci. Remote Sens.*, vol. 52, no. 5, pp. 2875–2888, May 2014.
[8] L. Pipia *et al.*, "Polarimetric differential SAR interferometry: First results with ground-based measurements," *IEEE Geosci. Remote Sens. Lett.*, vol. 6, no. 1, pp. 167–171, Jan. 2009.
[9] S. R. Cloude, *Polarisation: Applications in Remote Sensing*. Oxford, U.K.: Oxford Univ. Press, 2009.
[10] S. R. Cloude, "Uniqueness of target decomposition theorems in radar polarimetry," *Direct Inverse Methods Radar Polarimetry,* vol. 350, pp. 267–296, 1992.
[11] S. R. Cloude and E. Pottier, "Concept of polarization entropy in optical scattering," *Opt. Eng.*, vol. 34, no. 6, pp. 1599–1611, 1995.
[12] J. S. Lee and E. Pottier, *Polarimetric Radar Imaging: From basics to Applications*. Boca, Raton, FL, USA: CRC Press, 2009.
[13] F. Weissgerber, E. Colin-Koeniguer, N. Trouvé, and J. M. Nicolas, "A temporal estimation of entropy and its comparison with spatial estimations on PolSAR images," *IEEE J. Sel. Topics Appl. Earth Observ. Remote Sens.*, vol. 9, no. 8, pp. 3809–3820, Aug. 2016.
[14] C. Xu, S. Ma, Z. Tan, C. Xie, S. Toda, and X. Huang, "Landslides triggered by the 2016 Mj 7.3 Kumamoto, Japan, earthquake," *Landslides*, vol. 15, no. 3, pp. 551–564, Aug. 2018.
[15] A. Karunathilake, L. Zou, K. Kikuta, M. Nishimoto, and M. Sato, "Implementation and configuration of GB-SAR for landslide monitoring: Case study in Minami-Aso, Kumamoto," *Explor. Geophys.*, vol. 50, no. 2, pp. 210–220, 2019.
[16] S. R. Cloude and E. Pottier, "A review of target decomposition theorems in radar polarimetry," *IEEE Trans. Geosci. Remote Sens.*, vol. 34, no. 2, pp. 498–518, Mar. 1996.
[17] J. S. Lee, T. L. Ainsworth, J. P. Kelly, and C. Lopez-Martinez, "Evaluation and bias removal of multilook effect on entropy/alpha/anisotropy in polarimetric SAR decomposition," *IEEE Trans. Geosci. Remote Sens.*, vol. 46, no. 10, pp. 3039–3052, Oct. 2008.
[18] J. M. Lopez-Sanchez, J. Fortuny, S. R. Cloude, and A. J. Sieber, "Indoor polarimetric radar measurements on vegetation samples at L, S, C and X band," *J. Electromagn. Waves Appl.*, vol. 14, no. 2, pp. 205–231, 2000.
[19] S. R. Cloude and E. Pottier, "An entropy based classification scheme for land applications of polarimetric SAR," *IEEE Trans. Geosci. Remote Sens.*, vol. 35, no. 1, pp. 68–78, Jan. 1997.
[20] V. N. Bringi and V. Chandrasekar, *Polarimetric Doppler Weather Radar*. Cambridge, U.K.: Cambridge Univ. Press, 2001.
[21] J. P. Fritz and V. Chandrasekar, "A fully polarimetric characterization of the impact of precipitation on short wavelength synthetic aperture radar," *IEEE Trans. Geosci. Remote Sens.*, vol. 50, no. 5, pp. 2037–2048, May 2012.
[22] M. Montopoli, G. Botta, and F. S. Marzano, "Modeling polarimetric microwave propagation parameters from globally distributed raindrop size distribution measurements," in *Proc. Eur. Conf. Antennas Propag.*, 2009, pp. 1941–1945.
[23] I. Hajnsek, E. Pottier, and S. R. Cloude, "Inversion of surface parameters from polarimetric SAR," *IEEE Trans. Geosci. Remote Sens.*, vol. 41, no. 4, pp. 727–744, Apr. 2003.

[24] J. S. Lee, M. R. Grunes, D. L. Schuler, E. Pottier, and L. Ferro-Famil, "Scattering-model-based speckle filtering of polarimetric SAR data," *IEEE Trans. Geosci. Remote Sens.*, vol. 44, no. 1, pp. 176–187, Jan. 2006.
[25] A. Freeman, "Calibration of linearly polarized polarimetric SAR data subject to Faraday rotation," *IEEE Trans. Geosci. Remote Sens.*, vol. 42, no. 8, pp. 1617–1624, Aug. 2004.
[26] A. G. Fore *et al.*, "UAVSAR polarimetric calibration," *IEEE Trans. Geosci. Remote Sens.*, vol. 53, no. 6, pp. 3481–3491, Jun. 2015.
[27] J. J. Van Zyl, "Calibration of polarimetric radar images using only image parameters and trihedral corner reflector responses," *IEEE Trans. Geosci. Remote Sens.*, vol. 28, no. 3, pp. 337–348, May 1990.

Yuta Izumi (Student Member, IEEE) received the B.Eng. and M.Eng. degrees from Chiba University, Japan, in 2016, and 2018, respectively. He is currently working toward the Ph.D. degree with the Tohoku University, Japan.

His research interests include radar interferometry and polarimetry and their applications for disaster mitigation.

Mr. Izumi received the Young Researcher Award from IEEE Geoscience and Remote Sensing Society All Japan Joint Chapter. He was a recipient of the President Award of Chiba University and the Dean Award of the Graduate School of Advanced Integration Science, Chiba University, in 2018.

Motoyuki Sato (Fellow, IEEE) received the B.E., M.E., and Dr.Eng. degrees in information engineering from Tohoku University, Sendai, Japan, in 1980, 1982, and 1985, respectively.

Since 1997, he has been a Professor at Tohoku University and a Distinguished Professor of Tohoku University 2007–2011, the Director of Center for Northeast Asian Studies, Tohoku University 2009–2013. He was a Visiting Researcher with the Federal German Institute for Geoscience and Natural Resources in Hannover, Germany, in 1988–1989. His current interests include transient electromagnetics and antennas, radar polarimetry, ground penetrating radar (GPR), borehole radar, electromagnetic induction sensing, GB-SAR, and MIMO radar systems. He developed GPR sensors for humanitarian demining, and they are used in mine affected countries including Cambodia.

He received 2014 Frank Frischknecht Leadership Award from SEG for his contribution to his sustained and important contributions to near-surface geophysics in the field of ground-penetrating radar. He received IEICE Best Paper Award (Kiyasu Award) in 2017, Achievement Award in 2019, IEEE GRSS Education Award in 2012, and IEEE Ulrich L. Rohde innovative conference paper awards on Antenna Measurements and Applications in 2017. He was a Visiting Professor at Jilin University, China, Delft University of Technology, The Netherlands, and Mongolian University of Science and Technology.

Dr. Sato was a member of the IEEE GRSS AdCom (2006–2014). He is the Chair of IEEE Sendai Section in 2020–2021. He was an Associate Editor of IEEE GEOSCIENCE AND REMOTE SENSING LETTERS, and a Guest Editor of the special issue of GPR2006 and GPR2010 in TRANSACTIONS ON GEOSCIENCE AND REMOTE SENSING, and IGARSS2011, GPR2012, and GPR2014 in IEEE JOURNAL OF SELECTED TOPICS IN APPLIED ERATH OBSERVATIONS AND REMOTE SENSING. He was the Chair of the IEEE GRSS Japan Chapter (2006–2007). He served the General Chair of IGARSS2011 and the Technical Chair of GPR1996.